Available online at www.sciencedirect.com
SCIENCE DIRECT®
ELSEVIER Computers and Mathematics with Applications 51 (2006) 1349–1366
An International Journal
computers & mathematics with applications
www.elsevier.com/locate/camwa

Enriched Meshfree Collocation Method with Diffuse Derivatives for Elastic Fracture

YOUNG-CHEOL YOON
Department of Mechanical Engineering, Northwestern University
2145 Sheridan Road
Evanston, IL 60208-3111, U.S.A.
y-yoon@northwestern.edu

SANG-HO LEE
School of Civil & Environmental Engineering, Yonsei University
134 Shinchon-Dong, Seodaemoon-Ku
Seoul 120-749, Korea
lee@yonsei.ac.kr

T. BELYTSCHKO*
Department of Mechanical Engineering, Northwestern University
2145 Sheridan Road
Evanston, IL 60208-3111, U.S.A.
tedbelytschko@northwestern.edu

Abstract—A meshfree collocation method with intrinsic enrichment for solving elastic crack problems is presented. A diffuse derivative approximation is applied in conjunction with an intrinsic enrichment of the near-tip asymptotic fields and a polynomial basis. These consistent diffuse derivatives of the approximation do not require computing the derivative of the weight function or that of the moment matrix. The local behavior of the near-tip stresses is successfully captured so that the stress intensity factors can be accurately computed. Numerical experiments demonstrate the accuracy and robustness of the method for solving elastic fracture problems. © 2006 Elsevier Ltd. All rights reserved.

Keywords—Meshfree collocation method, Intrinsic enrichment, Diffuse derivatives.

1. INTRODUCTION

One of the attractive features of meshfree methods based on moving least squares (MLS) approximations in applications to elastic fracture problems is that excellent accuracy can be obtained by including the near-tip asymptotic field in the basis (see [1,2]). The near-tip fields need to be added to the basis only locally, so the cost is quite low. Recently, increasing interest has developed in employing collocation methods to elastic problems [3], since these methods avoid the quadrature of the weak form, and while not as accurate as Galerkin methods for a given number of unknowns, they tend to deliver more accuracy for the same computational effort when

*Author to whom all correspondence should be addressed.
The support of the Office of Naval Research (N00014-03-1-0097) and the Korean Research Foundation Grant (KRF-2004-042-D00189) are gratefully acknowledged.

doi:10.1016/j.camwa.2006.04.010

applied with the diffuse derivative techniques originally proposed by Nayroles *et al.* [4]. In the diffuse derivative approximation, only the derivatives of the polynomial basis need to be included in computing the gradients of the field variables. While the savings would at first appear to be small, they are quite substantial in collocation methods for second-order PDEs where second derivatives are required. For second-order PDEs, the fast methods for derivative computation given in [5] are still relatively time consuming. It should be noted that diffuse derivatives are not as attractive in Galerkin methods because they degrade the accuracy substantially [5,6]. Reviews of meshfree methods can be found in [7,8], so we will only touch on a few relevant works.

Enrichment of the basis was first proposed in the element-free Galerkin (EFG) method [9], a method that employs MLS approximants. The EFG method has been actively applied to many practical engineering problems, especially to crack propagation [10–12]. EFG without enrichment needs considerable nodal refinement to capture the singular stresses at the tip. However, enriched approximations have successfully modeled the near-tip field [1,2]. A method for enrichment based on the concept of partition of unity [13], a local type of enrichment, was suggested by Ventura *et al.* [14]. They combined the local enrichment technique with a vector level set to describe the evolution of crack discontinuity. Lee and Yoon [15] proposed a locally enriched EFG approximation combined with the visibility criterion for discontinuity modeling.

The diffuse derivative technique has been implemented in several collocation formulations. Kim and Kim [16] applied the method to solving fluid problems and proved the convergence of the derivative approximation in the L^p-norm, which justifies the use of diffuse derivative approximations with the strong forms of the governing equations. Huerta *et al.* [7] showed that diffuse derivatives converge to the exact derivatives. Lee and Yoon [3] employed the method in elasticity and linear elastic fracture problems. In solving fracture problems, they used the regular diffuse approximation without enrichment for treating near-tip field.

This paper presents a local intrinsic enrichment similar to [1,2] for a collocation method with a diffuse derivative approximation. The intent is to explore whether the diffuse derivative methods combined with collocation retain their relatively good accuracy for singular enrichments. The enrichment functions are here embedded in the basis set and the diffuse derivatives of the approximation are calculated by taking derivatives only of the basis. It is shown that this method successfully models near-tip fields with the $r^{-1/2}$ singularity in the derivative field. Therefore, the numerical scheme can provide efficient solutions of elastic crack problems and accurate stress intensity factors.

2. ENRICHED DIFFUSE DERIVATIVE APPROXIMATION

2.1. Intrinsic Enrichment of Diffuse Derivative Approximation for Near-Tip Fields

For convenience, we consider multi-index notation throughout this paper, so

$$\mathbf{x}^{\boldsymbol{\alpha}} := x_1^{\alpha_1} x_2^{\alpha_2} \cdots x_n^{\alpha_n}, \tag{1}$$

where $\boldsymbol{\alpha} = [\alpha_1, \ldots, \alpha_n]$ and n denotes the space dimension. A factorial in multi-index notation is defined by $\boldsymbol{\alpha} := \prod_{i=1}^{n} \alpha_i!$ and $|\boldsymbol{\alpha}| = \sum_{i=1}^{n} \alpha_i$. The α^{th} derivative of a function $f(\mathbf{x})$ with respect to $\mathbf{x}$ is defined by a differential operator $D_{\mathbf{x}}^{\boldsymbol{\alpha}}$ as follows:

$$D_{\mathbf{x}}^{\boldsymbol{\alpha}} f := \frac{\partial^{|\boldsymbol{\alpha}|} f}{\partial x_1^{\alpha_1} \partial x_2^{\alpha_2} \cdots \partial x_n^{\alpha_n}}. \tag{2}$$

Consider a cracked body Ω. (See Figure 1.) It can be divided into the regular domain Ω^R and the singular domain Ω^S. The singular domain consists of $\bigcup_{i=1}^{N_{\text{tip}}} \Omega_i^S$ where N_{tip} is the number of crack tips; the regular domain is denoted by $\Omega \setminus \Omega^S$. The asymptotic near-tip field displacement can be written as

$$u_i(r, \theta) \sim r^{1/2} F_i(\theta), \qquad i = 1, \ldots, n, \tag{3}$$

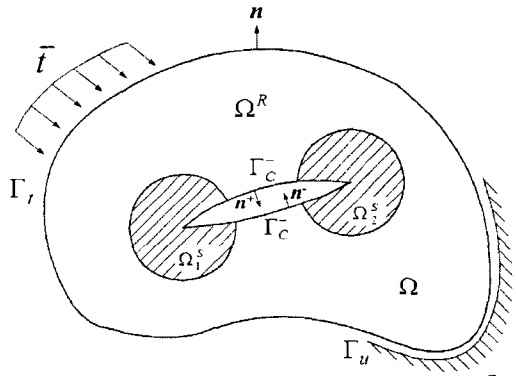

Figure 1. Cracked body Ω which consists of the singular domain Ω^S and the regular domain Ω^R bounded by $\Gamma_t \cup \Gamma_t \cup \Gamma_C$.

where $F_i(\theta)$ is determined by factors such as geometry, crack length, and loading; however, in all cases we use a near-tip field associated with a crack in an infinite body. The strength of the singularity in the derivative field is given by the coefficient $r^{-1/2}$ as $r \to 0$.

Let $u(\mathbf{x})$ be a continuous function in $\bar{\Omega}$. The displacement can then be decomposed into the regular and singular parts by

$$u(\mathbf{x}) := u^R(\mathbf{x}) + u^S(\mathbf{x}). \tag{4}$$

The singular part $u^S(\mathbf{x})$ will be designed to exhibit the asymptotic behavior given in (3). On the other hand, the regular part of $u(\mathbf{x})$ is given by

$$u^R(\mathbf{x}) := u(\mathbf{x}) - u^S(\mathbf{x}) \in C^m\left(\bar{\Omega}\right). \tag{5}$$

The regular part $u^R(\mathbf{x})$ can be approximated by a polynomial basis; the singular part is expressed by adding a singular enrichment function to the basis set.

Let $\mathbf{p}_m^\top(\mathbf{x})$ be a polynomial basis of order m, which is constructed from elements of a set P^m defined as

$$P^m := \left\{\mathbf{x}^\alpha = x_1^{\alpha_1} \cdots x_n^{\alpha_n} \mid |\alpha| = \alpha_1 + \cdots + \alpha_n \le m\right\}. \tag{6}$$

This set includes a complete basis of the subspace of polynomials of order m. For example, for $n = 2$, the polynomial basis vector can be written as

$$\mathbf{p}_m^\top(\mathbf{x}) = \left(1, x_1, x_2, x_2^2, x_1x_2, x_2^2, \ldots, x_2^m\right), \tag{7}$$

where the dimension of $\mathbf{p}_m(\mathbf{x}) \in P^m$ is $(n+m)!/n!m!$. In the domain Ω^R, $u(\mathbf{x})$ can be approximated by

$$u_L^R(\mathbf{x}, \bar{\mathbf{x}}) := \mathbf{p}_m^\top\left(\frac{\mathbf{x} - \bar{\mathbf{x}}}{\rho_{\bar{\mathbf{x}}}}\right)\mathbf{a}(\bar{\mathbf{x}}), \qquad \bar{\mathbf{x}} \in \Omega^R, \tag{8}$$

where $a(\bar{\mathbf{x}}) = (a_0(\bar{\mathbf{x}}), a_1(\bar{\mathbf{x}}), \ldots)$ is the unknown coefficient vector; $\rho_{\bar{\mathbf{x}}}$ is the dilation function, which varies in accordance with node density and is required to be continuous in $\bar{\Omega}$.

The singular part of $u(\mathbf{x})$ is approximated by functions taken from the Westergaard solution as in [1,2]

$$\begin{aligned}\mathbf{b}_{\text{tip}}^\top(\mathbf{x}) &= \left(b_{\text{tip}}^1(\mathbf{x} - \mathbf{x}_{\text{tip}}), b_{\text{tip}}^2(\mathbf{x} - \mathbf{x}_{\text{tip}}), b_{\text{tip}}^3(\mathbf{x} - \mathbf{x}_{\text{tip}}), b_{\text{tip}}^4(\mathbf{x} - \mathbf{x}_{\text{tip}})\right) \\ &= \left(r^{1/2}\sin\frac{\theta}{2}, r^{1/2}\cos\frac{\theta}{2}, r^{1/2}\sin\frac{\theta}{2}\sin\theta, r^{1/2}\cos\frac{\theta}{2}\sin\theta\right),\end{aligned} \tag{9}$$

where $r = \|\mathbf{x} - \mathbf{x}_{\text{tip}}\|$, θ is the angle measured from the tangent to the crack at the tip, and $\mathbf{x}_{\text{tip}}$ is the position of the crack tip. So, the singular part approximation can be written as

$$u_L^S(\mathbf{x}, \bar{\mathbf{x}}) := \mathbf{b}_{\text{tip}}^\top(\mathbf{x})\mathbf{c}(\bar{\mathbf{x}}), \tag{10}$$

where $\mathbf{c}(\bar{\mathbf{x}}) = (c_1(\bar{\mathbf{x}}), \ldots, c_4(\bar{\mathbf{x}}))$ is the unknown coefficient vector.

In the singular domain Ω^S, we use an enriched approximation defined by

$$u_L^{\text{en}}(\mathbf{x}, \bar{\mathbf{x}}) := u_L^R(\mathbf{x}, \bar{\mathbf{x}}) + u_L^S(\mathbf{x}, \bar{\mathbf{x}}), \qquad \bar{\mathbf{x}} \in \Omega^S, \tag{11}$$

where the derivative of the above approximation exhibits a singularity with strength $r^{-1/2}$. In the computation, the enriched approximation is used whenever the domain of influence of $\bar{\mathbf{x}}$ includes the tip. Equation (11) can be rewritten in terms of enriched vectors as follows:

$$u_L^{\text{en}}(\mathbf{x}, \bar{\mathbf{x}}) := \mathbf{p}_{\text{en}}^{\top}(\mathbf{x}, \bar{\mathbf{x}}) \mathbf{a}_{\text{en}}(\bar{\mathbf{x}}), \tag{12}$$

where $\mathbf{p}_{\text{en}}^{\top}(\mathbf{x}, \bar{\mathbf{x}}) = (\mathbf{p}_m^{\top}((\mathbf{x} - \bar{\mathbf{x}})/\rho), \mathbf{b}_{\text{tip}}^{\top}(\mathbf{x}))$ and $\mathbf{a}_{\text{en}}(\bar{\mathbf{x}}) = (\mathbf{a}(\bar{\mathbf{x}}), \mathbf{c}(\bar{\mathbf{x}}))^{\top}$.

To express the unknown coefficient vector, $\mathbf{a}_{\text{en}}(\bar{\mathbf{x}})$, in terms of nodal parameters, the standard MLS technique is used. A discrete weighted square functional is defined as

$$J := \sum_{I \in \Lambda_{\bar{\mathbf{x}}}} w\left(\frac{\mathbf{x}_{\text{I}} - \bar{\mathbf{x}}}{\rho_{\bar{\mathbf{x}}}}\right) \left[\mathbf{p}_{\text{en}}^{\top}(\mathbf{x}_{\text{I}}, \bar{\mathbf{x}})\, \mathbf{a}_{\text{en}}(\bar{\mathbf{x}}) - u_{\text{I}}\right]^2, \tag{13}$$

where $w((\mathbf{x}_{\text{I}} - \bar{\mathbf{x}})/\rho_{\bar{\mathbf{x}}})$ is the weight function which has compact support and u_{I} are nodal parameters. $\Lambda_{\bar{\mathbf{x}}}$ is the index set of nodes in the support of the weight function, i.e.,

$$\Lambda_{\bar{\mathbf{x}}} := \{I \in \Lambda_{\text{tot}} \mid \|\mathbf{x}_{\text{I}} - \bar{\mathbf{x}}\| < \rho_{\bar{\mathbf{x}}}\}, \tag{14}$$

where Λ_{tot} is the total set of nodes. Minimizing the residual functional J yields a normal equation

$$\mathbf{M}(\bar{\mathbf{x}}) \mathbf{a}_{\text{en}}(\bar{\mathbf{x}}) - \mathbf{P}^{\top}(\bar{\mathbf{x}}) \mathbf{W}(\bar{\mathbf{x}}) \hat{\mathbf{u}} = 0, \tag{15}$$

where $\hat{\mathbf{u}} = \{u_1, u_2, \ldots, u_N\}^{\top}$ is a vector of nodal variables, and $\mathbf{P}(\bar{\mathbf{x}})$ is

$$\begin{aligned} \mathbf{P}(\bar{\mathbf{x}}) &= \begin{bmatrix} \mathbf{p}_m^{\top}\left(\dfrac{\mathbf{x}_1 - \bar{\mathbf{x}}}{\boldsymbol{\rho}}\right) & \mathbf{b}_{\text{tip}}^{\top}(\mathbf{x}_1) \\ \vdots & \vdots \\ \mathbf{p}_m^{\top}\left(\dfrac{\mathbf{x}_N - \bar{\mathbf{x}}}{\boldsymbol{\rho}}\right) & \mathbf{b}_{\text{tip}}^{\top}(\mathbf{x}_N) \end{bmatrix} \\ &= \begin{bmatrix} 1 & \cdots & \left(\dfrac{\mathbf{x}_1 - \bar{\mathbf{x}}}{\boldsymbol{\rho}}\right)^{\mathbf{m}} & b_{\text{tip}}^1(\mathbf{x}_1 - \mathbf{x}_{\text{tip}}) & \cdots & b_{\text{tip}}^4(\mathbf{x}_1 - \mathbf{x}_{\text{tip}}) \\ \vdots & \ddots & \vdots & \vdots & \ddots & \vdots \\ 1 & \cdots & \left(\dfrac{\mathbf{x}_N - \bar{\mathbf{x}}}{\boldsymbol{\rho}}\right)^{\mathbf{m}} & b_{\text{tip}}^1(\mathbf{x}_N - \mathbf{x}_{\text{tip}}) & \cdots & b_{\text{tip}}^4(\bar{\mathbf{x}}_N - \mathbf{x}_{\text{tip}}) \end{bmatrix}. \end{aligned} \tag{16}$$

The matrix $\mathbf{W}(\bar{\mathbf{x}})$ is a diagonal matrix consisting of the weight functions

$$\mathbf{W}(\bar{\mathbf{x}}) = \begin{bmatrix} w\left(\dfrac{\mathbf{x}_1 - \bar{\mathbf{x}}}{\rho_{\bar{\mathbf{x}}}}\right) & \cdots & 0 \\ \vdots & \ddots & \vdots \\ 0 & \cdots & w\left(\dfrac{\mathbf{x}_N - \bar{\mathbf{x}}}{\rho_{\bar{\mathbf{x}}}}\right) \end{bmatrix}. \tag{17}$$

The moment matrix $\mathbf{M}(\bar{\mathbf{x}})$ can be written as

$$\mathbf{M}(\bar{\mathbf{x}}) = \mathbf{P}^{\top}(\bar{\mathbf{x}}) \mathbf{W}(\bar{\mathbf{x}}) \mathbf{P}(\bar{\mathbf{x}}). \tag{18}$$

The unknown coefficients $\mathbf{a}_{\text{en}}(\bar{\mathbf{x}})$ are obtained by rearranging the normal equation

$$\mathbf{a}_{\text{en}}(\bar{\mathbf{x}}) = \mathbf{M}^{-1}(\bar{\mathbf{x}}) \mathbf{P}^{\top}(\bar{\mathbf{x}}) \mathbf{W}(\bar{\mathbf{x}}) \hat{\mathbf{u}}. \tag{19}$$

As a consequence, the enriched local approximation of $u(\mathbf{x})$ is given by

$$u_L^{\text{en}}(\mathbf{x},\bar{\mathbf{x}}) = \mathbf{p}_{\text{en}}^{\top}(\mathbf{x},\bar{\mathbf{x}})\mathbf{M}^{-1}(\bar{\mathbf{x}})\mathbf{P}^{\top}(\bar{\mathbf{x}})\mathbf{W}(\bar{\mathbf{x}})\hat{\mathbf{u}}. \tag{20}$$

Let us consider the diffuse derivative operator which consists of the differentiation with respect to $\mathbf{x}$ and the limiting process as $\bar{\mathbf{x}}$ goes to $\mathbf{x}$,

$$\mathfrak{D}_{\mathbf{x}}^{\boldsymbol{\alpha}}\left(f(\mathbf{x},\bar{\mathbf{x}})\right) := \lim_{\bar{\mathbf{x}}\to\mathbf{x}}\left\{D_{\mathbf{x}}^{\boldsymbol{\alpha}}\left(f(\mathbf{x},\bar{\mathbf{x}})\right)\right\} = \lim_{\bar{\mathbf{x}}\to\mathbf{x}}\left\{\frac{\partial^{|\boldsymbol{\alpha}|}\left(f(\mathbf{x},\bar{\mathbf{x}})\right)}{\partial x_1^{\alpha_1}\,\partial x_2^{\alpha_2}\cdots\partial x_n^{\alpha_n}}\right\}, \tag{21}$$

where the differentiation is taken prior to the limiting process; a similar definition of the diffuse derivative approximation was suggested by Nayroles *et al.* [4] for a polynomial basis. The derivatives of the enriched local approximation are obtained by

$$\begin{aligned}\mathfrak{D}_{\mathbf{x}}^{\boldsymbol{\alpha}}u(\mathbf{x}) &:= \lim_{\bar{\mathbf{x}}\to\mathbf{x}}\left(D_{\mathbf{x}}^{\boldsymbol{\alpha}}u_L^{\text{en}}(\mathbf{x},\bar{\mathbf{x}})\right)\\ &= \lim_{\bar{\mathbf{x}}\to\mathbf{x}}\left\{D_{\mathbf{x}}^{\boldsymbol{\alpha}}\left(\mathbf{p}_{\text{en}}^{\top}(\mathbf{x},\bar{\mathbf{x}})\right)\mathbf{M}^{-1}(\bar{\mathbf{x}})\mathbf{P}^{\top}(\bar{\mathbf{x}})\mathbf{W}(\bar{\mathbf{x}})\hat{\mathbf{u}}\right\}, \qquad |\boldsymbol{\alpha}| \le m.\end{aligned} \tag{22}$$

Thus, the derivatives of $u(\mathbf{x})$ can be approximated by the diffuse derivative

$$D_{\mathbf{x}}^{\boldsymbol{\alpha}}u(\mathbf{x}) \approx \mathfrak{D}_{\mathbf{x}}^{\boldsymbol{\alpha}}u(\mathbf{x}). \tag{23}$$

Collecting all the diffuse derivatives of the enriched local approximation up to the order m yields

$$\begin{pmatrix}\mathfrak{D}_{\mathbf{x}}^{[0,0]}u(\mathbf{x})\\ \vdots\\ \mathfrak{D}_{\mathbf{x}}^{[0,m]}u(\mathbf{x})\end{pmatrix} := \begin{pmatrix}\lim\limits_{\bar{\mathbf{x}}\to\mathbf{x}} D_{\mathbf{x}}^{[0,0]}\left(u_L^{\text{en}}(\mathbf{x},\bar{\mathbf{x}})\right)\\ \vdots\\ \lim\limits_{\bar{\mathbf{x}}\to\mathbf{x}} D_{\mathbf{x}}^{[0,m]}\left(u_L^{\text{en}}(\mathbf{x},\bar{\mathbf{x}})\right)\end{pmatrix} = \mathbf{Q}_{\text{en}}(\mathbf{x})\mathbf{M}^{-1}(\mathbf{x})\mathbf{P}^{\top}(\mathbf{x})\mathbf{W}(\mathbf{x})\hat{\mathbf{u}}, \tag{24}$$

where the matrix $\mathbf{Q}_{\text{en}}(\mathbf{x})$ is defined by

$$\begin{aligned}\mathbf{Q}_{\text{en}}(\mathbf{x}) &:= \begin{pmatrix}\lim\limits_{\bar{\mathbf{x}}\to\mathbf{x}} D_{\mathbf{x}}^{[0,0]}\mathbf{p}_{\text{en}}^{\top}(\mathbf{x},\bar{\mathbf{x}})\\ \vdots\\ \lim\limits_{\bar{\mathbf{x}}\to\mathbf{x}} D_{\mathbf{x}}^{[0,m]}\mathbf{p}_{\text{en}}^{\top}(\mathbf{x},\bar{\mathbf{x}})\end{pmatrix}\\ &= \begin{pmatrix}1 & \cdots & 0 & b_{\text{tip}}^1(\mathbf{x}-\mathbf{x}_{\text{tip}}) & \cdots & b_{\text{tip}}^4(\mathbf{x}-\mathbf{x}_{\text{tip}})\\ \vdots & \ddots & \vdots & \vdots & \ddots & \vdots\\ 0 & \cdots & \dfrac{m!}{\rho^m} & D_{\mathbf{x}}^{[0,m]}b_{\text{tip}}^1(\mathbf{x}-\mathbf{x}_{\text{tip}}) & \cdots & D_{\mathbf{x}}^{[0,m]}b_{\text{tip}}^4(\mathbf{x}-\mathbf{x}_{\text{tip}})\end{pmatrix}.\end{aligned} \tag{25}$$

Also, collecting the diffuse derivatives of the nodal shape functions up to order m gives

$$\begin{pmatrix}\Phi_1^{[0,0]}(\mathbf{x}) & \cdots & \Phi_N^{[0,0]}(\mathbf{x})\\ \vdots & \ddots & \vdots\\ \Phi_1^{[0,m]}(\mathbf{x}) & \cdots & \Phi_N^{[0,m]}(\mathbf{x})\end{pmatrix} := \mathbf{Q}_{\text{en}}(\mathbf{x})\mathbf{M}^{-1}(\mathbf{x})\mathbf{P}^{\top}(\mathbf{x})\mathbf{W}(\mathbf{x}), \tag{26}$$

where α^{th} row contains the α^{th} derivatives of the shape functions while the I^{th} column includes all derivatives of the shape function for node I. In this study, different approximations are used according to the domain where the local center $\bar{\mathbf{x}}$ occurs. For $\bar{\mathbf{x}} \in \Omega^S$, the enriched diffuse derivative approximation is employed; for $\bar{\mathbf{x}} \in \Omega^R$, the regular diffuse derivative approximation was used. So, the shape function may be slightly discontinuous across the boundary between Ω^R and Ω^S. However it appears not to impair the accuracy. On the other hand, if a diffuse derivative

approximation is implemented in a Galerkin formulation, special treatments such as coupling [1,2] are required to circumvent the discontinuity of the shape function. The weak formulation requires the full derivative of the shape function for the accurate quadrature of the weak form [5,6].

2.2. Reproducing Property of the Enriched Diffuse Derivative Approximation

The enrichment functions given in (9) are designed to model the singular behavior of the first derivative of the near-tip field in domain Ω^S. The enriched diffuse derivative approximation has the reproducing property for any function that can be constructed from a linear combination of the basis. The displacement, strain, and stress can be computed in the computational domain by (22) (or (24)) combined with the kinematic and constitutive relation given in the next section. When nodal parameters are taken from the polynomial space P^m, the diffuse derivative approximation reproduces the original polynomial exactly. The reproducing condition for the polynomials and derivatives up to the order $\boldsymbol{\beta}$ can be written as

$$\sum_{\mathrm{I}} \Phi_{\mathrm{I}}^{[\boldsymbol{\alpha}]}(\mathbf{x}) \left(\frac{\mathbf{x}_{\mathrm{I}} - \mathbf{x}}{\rho_{\mathbf{x}}} \right)^{\boldsymbol{\beta}} = \frac{\boldsymbol{\alpha}!}{\rho_{\mathbf{x}}^{|\boldsymbol{\alpha}|}} \delta_{\alpha\beta}, \qquad |\boldsymbol{\alpha}|, |\boldsymbol{\beta}| \leq m. \tag{27}$$

The α^{th} derivative of shape function for node I is given by

$$\Phi_{\mathrm{I}}^{[\boldsymbol{\alpha}]}(\mathbf{x}) = \mathbf{e}_{\alpha}^{\top} \mathbf{Q}_{\mathrm{en}}(\mathbf{x}) \mathbf{M}^{-1}(\mathbf{x}) \mathbf{p}_{\mathrm{en}}(\mathbf{x}_{\mathrm{I}}, \mathbf{x}) w \left(\frac{\mathbf{x}_{\mathrm{I}} - \mathbf{x}}{\rho_{\mathbf{x}}} \right), \tag{28}$$

where $\mathbf{e}_{\alpha}^{\top} = (0, \ldots, 1, \ldots, 0)$ which have 1 at the α^{th} slot in lexicographic order. Also, the augmented vectors for the regular part and singular part can be written as

$$\mathbf{e}_{R,\alpha}^{\top} = (\mathbf{e}_{\alpha}^{\top}, \mathbf{0}_S^{\top}) = \left(\underbrace{0, \ldots, 1, \ldots, 0}_{\text{Regular part}}, \underbrace{0, 0, 0, 0}_{\text{Singular part}} \right), \tag{29}$$

and

$$\mathbf{e}_{S,k}^{\top} = (\mathbf{0}_R^{\top}, \mathbf{e}_k^{\top}) = \left(\underbrace{0, \ldots, 0}_{\text{Regular part}}, \underbrace{0, \ldots, 1, \ldots, 0}_{\text{Singular part}} \right), \tag{30}$$

where 1 is placed at the α^{th} or k^{th} slot of the augmented vector in lexicographic order. Then, since $((\mathbf{x}_{\mathrm{I}} - \mathbf{x})/\rho_{\mathbf{x}})^{\boldsymbol{\beta}} = \mathbf{p}_{\mathrm{en}}^{\top}(\mathbf{x}_{\mathrm{I}}, \mathbf{x}) \mathbf{e}_{R,\beta}$, substituting (28) into (27) yields

$$\begin{aligned} \sum_{\mathrm{I}} \Phi_{\mathrm{I}}^{[\boldsymbol{\alpha}]}(\mathbf{x}) \left(\frac{\mathbf{x}_{\mathrm{I}} - \mathbf{x}}{\rho_{\mathbf{x}}} \right)^{\boldsymbol{\beta}} &= \sum_{\mathrm{I}} \left(\mathbf{e}_{\alpha}^{\top} \mathbf{Q}_{\mathrm{en}}(\mathbf{x}) \mathbf{M}^{-1}(\mathbf{x}) \mathbf{p}_{\mathrm{en}}(\mathbf{x}_{\mathrm{I}}, \mathbf{x}) w \left(\frac{\mathbf{x}_{\mathrm{I}} - \mathbf{x}}{\rho_{\mathbf{x}}} \right) \right) \\ &\quad \cdot \mathbf{p}_{\mathrm{en}}^{\top}(\mathbf{x}_{\mathrm{I}}, \mathbf{x}) \mathbf{e}_{R,\beta} \\ &= \mathbf{e}_{\alpha}^{\top} \mathbf{Q}_{\mathrm{en}}(\mathbf{x}) \mathbf{e}_{R,\beta} = \lim_{\bar{\mathbf{x}} \to \mathbf{x}} \left\{ D_{\mathbf{x}}^{\boldsymbol{\alpha}} \mathbf{p}_{\mathrm{en}}^{\top}(\mathbf{x}, \bar{\mathbf{x}}) \right\} \mathbf{e}_{R,\beta} \\ &= \frac{\boldsymbol{\alpha}!}{\rho_{\mathbf{x}}^{|\boldsymbol{\alpha}|}} \delta_{\alpha\beta}, \end{aligned} \tag{31}$$

which completes the proof of the reproducing property for the polynomials basis.

An enriched diffuse derivative approximation also reproduces the enrichment functions that are included in the basis. The reproducing condition for the enrichment functions and their derivatives takes the form

$$\sum_{\mathrm{I}} \Phi_{\mathrm{I}}^{[\boldsymbol{\alpha}]}(\mathbf{x}) b_{\mathrm{tip}}^{k}(\mathbf{x}_{\mathrm{I}} - \mathbf{x}_{\mathrm{tip}}) = D_{\mathbf{x}}^{\boldsymbol{\alpha}} b_{\mathrm{tip}}^{k}(\mathbf{x} - \mathbf{x}_{\mathrm{tip}}), \qquad k = 1, \ldots, 4 \quad \text{and} \quad |\boldsymbol{\alpha}| \leq m, \tag{32}$$

where $b_{\mathrm{tip}}^{k}(\mathbf{x}_{\mathrm{I}} - \mathbf{x}_{\mathrm{tip}}) = \mathbf{p}_{\mathrm{en}}^{\top}(\mathbf{x}_{\mathrm{I}}, \mathbf{x}) \mathbf{e}_{S,k}$. Then we have

$$\begin{aligned}\sum_{\mathrm{I}} \Phi_{\mathrm{I}}^{[\boldsymbol{\alpha}]}(\mathbf{x}) b_{\mathrm{tip}}^{k}(\mathbf{x}_{\mathrm{I}}) &= \sum_{\mathrm{I}} \left(\mathbf{e}_{\alpha}^{\top} \mathbf{Q}_{\mathrm{en}}(\mathbf{x}) \mathbf{M}^{-1}(\mathbf{x}) \mathbf{p}_{\mathrm{en}}(\mathbf{x}_{\mathrm{I}}, \mathbf{x})\, w\left(\frac{\mathbf{x}_{\mathrm{I}} - \mathbf{x}}{\rho_{\mathbf{x}}} \right) \right) \mathbf{p}_{\mathrm{en}}^{\top}(\mathbf{x}_{\mathrm{I}}, \mathbf{x})\, \mathbf{e}_{S,k} \\ &= \mathbf{e}_{\alpha}^{\top} \mathbf{Q}_{\mathrm{en}}(\mathbf{x}) \mathbf{e}_{S,k} = \lim_{\bar{\mathbf{x}} \to \mathbf{x}} \left\{ D_{\mathbf{x}}^{\boldsymbol{\alpha}} \mathbf{p}_{\mathrm{en}}^{\top}(\mathbf{x}, \bar{\mathbf{x}}) \right\} \mathbf{e}_{S,k} \\ &= D_{\mathbf{x}}^{\boldsymbol{\alpha}} b_{\mathrm{tip}}^{k}(\mathbf{x} - \mathbf{x}_{\mathrm{tip}}).\end{aligned} \tag{33}$$

So the reproducing property of the enrichment function and derivatives is verified.

The reproducing property for the near-tip field can be numerically demonstrated. When the nodal parameters are given by the exact near-tip fields (see Table 1), the displacement and stress fields can be regenerated exactly. A square patch discretized with 225 nodes was used in the computation. Figures 2a and 2b and 3a and 3b show surface plots for the reproduced x- and y-displacements for Mode I and Mode II near-tip fields, respectively. The plots are generated using additional sampling points. Figures 4a and 4b and 5a and 5b show contour plots for the reproduced near-tip stresses for Mode I and Mode II, respectively. The stresses for Mode l are computed by

$$\hat{\sigma}_{11}^{l}(\mathbf{x}) = \sum_{\mathrm{I}} \left\{ (\lambda + 2\mu) \Phi_{\mathrm{I}}^{[1,0]}(\mathbf{x}) u_1^{l}(\mathbf{x}_{\mathrm{I}}) + \lambda \Phi_{\mathrm{I}}^{[0,1]}(\mathbf{x}) u_2^{l}(\mathbf{x}_{\mathrm{I}}) \right\}, \qquad l = \mathrm{I}, \mathrm{II}, \tag{34}$$

$$\hat{\sigma}_{22}^{l}(\mathbf{x}) = \sum_{\mathrm{I}} \left\{ (\lambda + 2\mu) \Phi_{\mathrm{I}}^{[0,1]}(\mathbf{x}) u_2^{l}(\mathbf{x}_{\mathrm{I}}) + \lambda \Phi_{\mathrm{I}}^{[1,0]}(\mathbf{x}) u_1^{l}(\mathbf{x}_{\mathrm{I}}) \right\}, \qquad l = \mathrm{I}, \mathrm{II}, \tag{35}$$

where the superposed bar '^' stands for the numerical solution. If we consider L^{∞} error which is defined by

Table 1. Asymptotic solution of near-tip fields for Mode I and II cracks where μ and κ are the Lamé constants.

Modes	Displacement Fields
Mode I	$u_1^{\mathrm{I}}(r,\theta) = \frac{K_{\mathrm{I}}}{2\mu}\sqrt{\frac{r}{2\pi}} \cos\left(\frac{\theta}{2}\right)\left[\kappa - 1 + 2\sin^2\left(\frac{\theta}{2}\right)\right]$
	$u_2^{\mathrm{I}}(r,\theta) = \frac{K_{\mathrm{I}}}{2\mu}\sqrt{\frac{r}{2\pi}} \sin\left(\frac{\theta}{2}\right)\left[\kappa + 1 - 2\cos^2\left(\frac{\theta}{2}\right)\right]$
Mode II	$u_1^{\mathrm{II}}(r,\theta) = \frac{K_{\mathrm{II}}}{2\mu}\sqrt{\frac{r}{2\pi}} \sin\left(\frac{\theta}{2}\right)\left[\kappa + 1 + 2\cos^2\left(\frac{\theta}{2}\right)\right]$
	$u_2^{\mathrm{II}}(r,\theta) = -\frac{K_{\mathrm{II}}}{2\mu}\sqrt{\frac{r}{2\pi}} \cos\left(\frac{\theta}{2}\right)\left[\kappa - 1 - 2\sin^2\left(\frac{\theta}{2}\right)\right]$

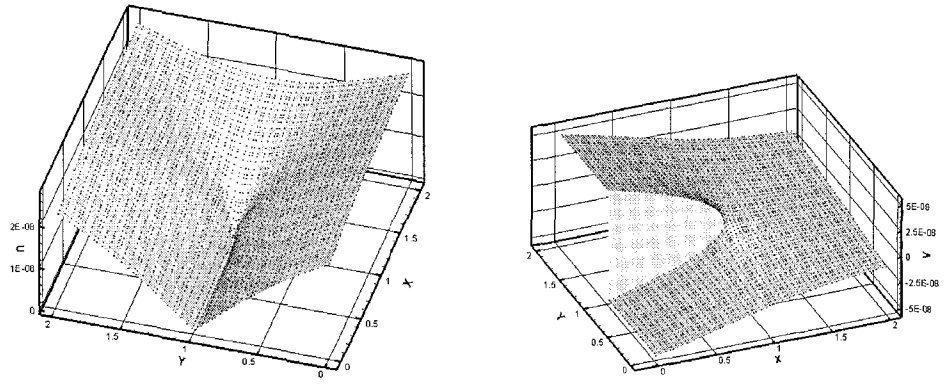

(a) $\sum_J \Phi_J^{[0,0]}(\mathbf{x}) u_1^{\mathrm{I}}(\mathbf{x}_J)$. (b) $\sum_J \Phi_J^{[0,0]}(\mathbf{x}) u_2^{\mathrm{I}}(\mathbf{x}_J)$.

Figure 2. Surface plots for the reproduced near-tip fields for Mode I.

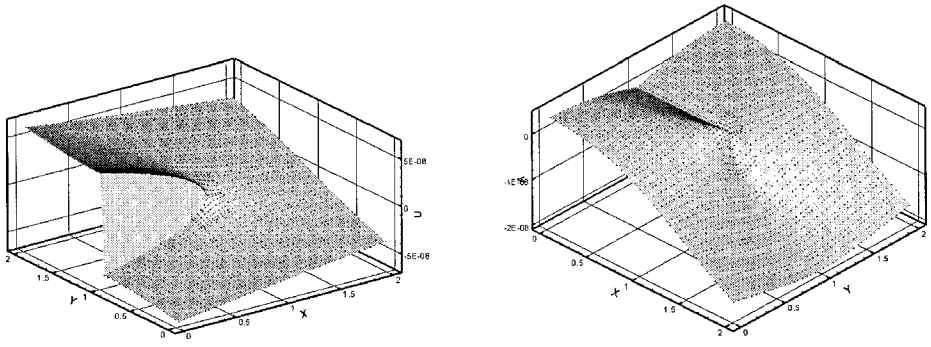

(a) $\sum_J \Phi_J^{[0,0]}(\mathbf{x}) u_1^{\mathrm{II}}(\mathbf{x}_J)$. (b) $\sum_J \Phi_J^{[0,0]}(\mathbf{x}) u_2^{\mathrm{II}}(\mathbf{x}_J)$.

Figure 3. Surface plots for the reproduced near-tip fields for Mode II.

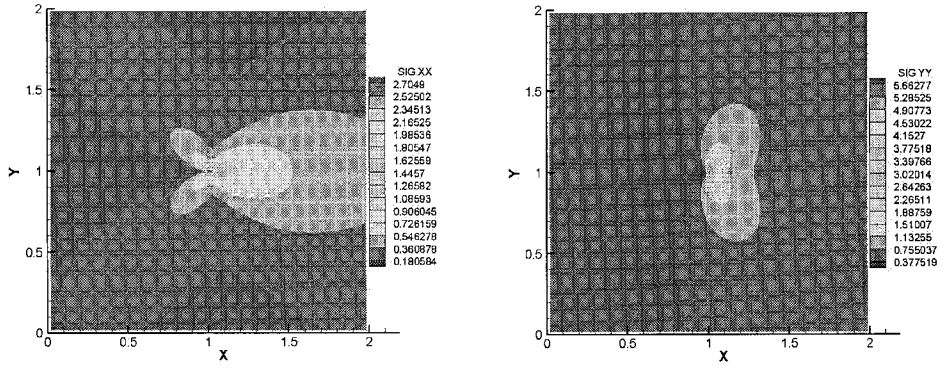

(a) $\sum_J \{(\lambda+2\mu)\Phi_J^{[1,0]}(\mathbf{x}) u_1^{\mathrm{I}}(\mathbf{x}_J) + \lambda \Phi_J^{[0,1]}(\mathbf{x}) u_2^{\mathrm{I}}(\mathbf{x}_J)\}$.

(b) $\sum_J \{(\lambda+2\mu)\Phi_J^{[0,1]}(\mathbf{x}) u_2^{\mathrm{I}}(\mathbf{x}_J) + \lambda \Phi_J^{[1,0]}(\mathbf{x}) u_1^{\mathrm{I}}(\mathbf{x}_J)\}$.

Figure 4. Contour plots for the reproduced near-tip stresses for Mode I.

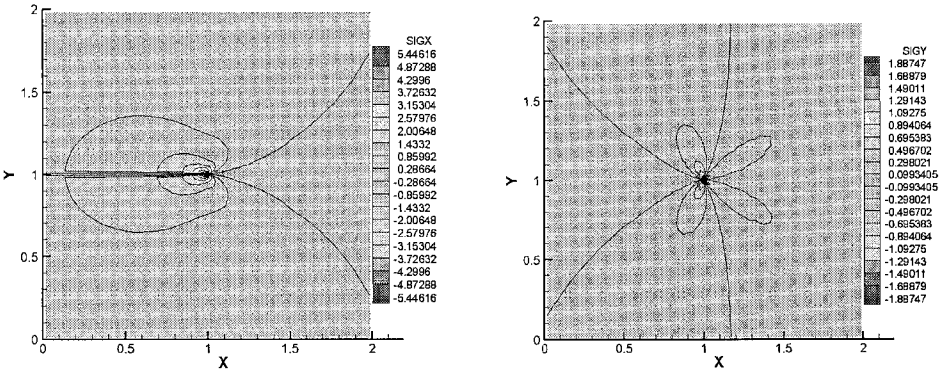

(a) $\sum_J \{(\lambda+2\mu)\Phi_J^{[1,0]}(\mathbf{x}) u_1^{\mathrm{II}}(\mathbf{x}_J) + \lambda \Phi_J^{[0,1]}(\mathbf{x}) u_2^{\mathrm{II}}(\mathbf{x}_J)\}$.

(b) $\sum_J \{(\lambda+2\mu)\Phi_J^{[0,1]}(\mathbf{x}) u_2^{\mathrm{II}}(\mathbf{x}_J) + \lambda \Phi_J^{[1,0]}(\mathbf{x}) u_1^{\mathrm{II}}(\mathbf{x}_J)\}$.

Figure 5. Contour plots for the reproduced near-tip stresses for Mode II.

$$\|e_u\|_{L^\infty} = \sum_{i=1}^{n} \frac{\max_{I \in \Lambda_{\mathrm{tot}}} \{|\hat{u}_i(\mathbf{x}_I) - u_i(\mathbf{x}_I)|\}}{\max_{J \in \Lambda_{\mathrm{tot}}} \{|u_i(\mathbf{x}_J)|\}}, \tag{36}$$

then we note that the errors in the reproducing displacement and stress are obtained in the range of the machine precision. The near-tip field can be reproduced exactly by the enriched diffuse derivative approximation.

3. DISCRETIZATION BASED ON STRONG FORMULATION

3.1. Governing Partial Differential Equations

Consider a linear elastic solid. The differential forms of the governing equations with displacement $\mathbf{u}$ and body forces $\mathbf{b}$ are

$$(\lambda+\mu)\nabla(\nabla\cdot\mathbf{u})+\mu\nabla^2\mathbf{u}=-\mathbf{b}, \qquad \text{in } \Omega, \tag{37}$$

$$\mathbf{u}=\bar{\mathbf{u}}, \qquad \text{on } \Gamma_u, \tag{38}$$

$$2\mu\mathbf{n}\cdot(\nabla_{\text{sym}}\mathbf{u})+\lambda\mathbf{n}\cdot\mathbf{1}\,(\nabla\cdot\mathbf{u})=\bar{\mathbf{t}}, \qquad \text{on } \Gamma_t \text{ and } \Gamma_C, \tag{39}$$

where $\nabla^2(=\nabla\cdot\nabla)$ denotes Laplace operator; $\mathbf{n}$ is the unit normal to the boundary Γ_t or $\Gamma_C(=\Gamma_C^+\cup\Gamma_C^-)$; ∇_{sym} is the symmetric part of the gradient operator; $\mathbf{1}=\delta_{ij}\mathbf{e}_i\otimes\mathbf{e}_j$ is a second-order identity tensor; λ and μ are the Lamé constants; $\bar{\mathbf{t}}$ is the prescribed traction vector. For isotropic elastic material with small strain, the strains and stresses are computed by the kinematic equations and the constitutive relation

$$\boldsymbol{\varepsilon}=\nabla_{\text{sym}}\mathbf{u}=\frac{1}{2}\left(\nabla\mathbf{u}+\nabla\mathbf{u}^{\top}\right), \tag{40}$$

$$\boldsymbol{\sigma}=2\mu\boldsymbol{\varepsilon}+\lambda\,\text{tr}(\boldsymbol{\varepsilon})\mathbf{1}, \tag{41}$$

where $\text{tr}(\boldsymbol{\varepsilon})$ is the trace of the strain tensor.

3.2. Discrete System for Strong Formulation

The strong formulation is discretized by a collocation method. Let Λ_u be the set of nodes on the essential boundary, Λ_t be the set of nodes on the natural boundaries including the crack surfaces, and Λ_{int} be the set of interior nodes not belonging to any boundary. Then $\Lambda_{\text{tot}}=\Lambda_{\text{int}}+\Lambda_t+\Lambda_u$ is the total set of nodes. The discrete equations are

$$\left\|\mathfrak{L}\mathbf{u}^h(\mathbf{x}_I)+\mathbf{b}(\mathbf{x}_I)\right\|_{L^\infty(\Omega)}=0, \qquad I\in\Lambda_{\text{int}}, \qquad \text{and} \quad \mathbf{x}_I\in\Omega^R\cup\Omega^S, \tag{42}$$

$$\left\|\mathfrak{B}_S\mathbf{u}^h(\mathbf{x}_J)-\bar{\mathbf{t}}(\mathbf{x}_J)\right\|_{L^\infty(\Gamma_t\cup\Gamma_C)}=0, \qquad J\in\Lambda_t\cup\Lambda_C, \quad \text{and} \quad \mathbf{x}_J\in\Gamma_t\cup\Gamma_C, \tag{43}$$

$$\left\|\mathfrak{B}_u\mathbf{u}^h(\mathbf{x}_K)-\bar{\mathbf{u}}(\mathbf{x}_K)\right\|_{L^\infty(\Gamma_u)}=0, \qquad K\in\Lambda_u, \qquad \text{and } \mathbf{x}_K\in\Gamma_u, \tag{44}$$

where the differential operators for the interior domain, natural boundary, and essential boundary are given by

$$\mathfrak{L}=(\lambda+\mu)\nabla\nabla\cdot+\mu\nabla^2, \tag{45}$$

$$\mathfrak{B}_t=2\mu\mathbf{n}\cdot\nabla_{\text{sym}}+\lambda\mathbf{n}\cdot\mathbf{1}\nabla\cdot, \tag{46}$$

$$\mathfrak{B}_{\text{u}}=\mathbf{1}\cdot. \tag{47}$$

Rearranging the above residual equations yields a discrete system

$$\mathbf{K}\cdot\mathbf{d}=\mathbf{F}, \tag{48}$$

where coefficient matrix $\mathbf{K}$ is banded but not symmetric. Matrices $\mathbf{K}$, $\mathbf{d}$, and $\mathbf{F}$ can be subdivided as follows:

$$\mathbf{K}=\begin{bmatrix}\mathbf{k}^{\text{int}}\\ \mathbf{k}^t\\ \mathbf{k}^u\end{bmatrix}, \qquad \mathbf{d}=\begin{pmatrix}\hat{\mathbf{u}}^{\text{int}}\\ \hat{\mathbf{u}}^t\\ \hat{\mathbf{u}}^u\end{pmatrix}, \qquad \text{and} \qquad \mathbf{F}=\begin{pmatrix}\mathbf{f}^{\text{int}}\\ \mathbf{f}^t\\ \mathbf{f}^u\end{pmatrix}, \tag{49}$$

where $\mathbf{k}^{\text{int}}$, $\mathbf{k}^t$, and $\mathbf{k}^u$ are coefficient matrices for the interior, natural boundary, and essential boundary nodes, respectively; $\hat{\mathbf{u}}^{\text{int}}$, $\hat{\mathbf{u}}^t$, and $\hat{\mathbf{u}}^u$ are the corresponding unknowns; $\mathbf{f}^{\text{int}}$, $\mathbf{f}^t$, and $\mathbf{f}^u$

are the corresponding force vectors. The residual equations should be linearly independent so that the coefficient matrix $\mathbf{K}$ is nonsingular. In parallel with meshfree collocation methods, applications of collocation schemes based on the radial basis function using symmetrical collocation can also be referred to [17].

For crack modeling, the traction-free condition is imposed along the nodes placed on the crack surfaces. To describe the crack trajectory, a series of straight line segments is introduced here, though for more generality, level set techniques such as given in [14] are desirable. Crack surfaces Γ_C are generated by placing nodes on both sides of the line segments. The crack path is tracked by updating this node arrangement and advancing the line segments as in [3]. The displacement discontinuity due to a crack is modeled by so-called visibility criterion [1,2]. The visibility criterion cuts the domain of influence of nodes with respect to the line segment representation. When the domain of influence is slit by a crack, the diffraction method or wrap-around method [1,2] is employed; abrupt changes in the size of domain of influence or the support of weight function can be avoided so that a smooth approximation is achieved around the crack tip.

4. NUMERICAL EXAMPLES

4.1. Square Patch with Near-Tip Fields

A cracked square patch with boundary conditions from the closed-form solution for Mode I and Mode II cracks is considered. Along the boundaries of the patch, the known near-tip displacement fields are prescribed. The computed displacement and stress fields are compared with the closed-form solution. Figure 6 illustrates the square patch with dimensions $2a \times 2a$ that includes a crack of length a. The crack tip is located at the center of the patch, (a, a) for the convergence test. Models of 85, 232, and 637 nodes (regularly distributed in the model without densification around the tip) are considered. Also, Figure 7 shows a node model which is densified around the tip and is employed for studies with a polynomial basis without enrichment. To capture the near-tip field, nodes are concentrated near the tip with aspect ratio (maximum and minimum nodal spacing $(h_{\max}/h_{\min})$) of 10.

The closed-form solutions are already given in Table 1. After the stress intensity factor is prescribed by $K_{\mathrm{I}}^{\mathrm{pres}} = 1$, the resultant stress intensity factor is calculated by an interaction

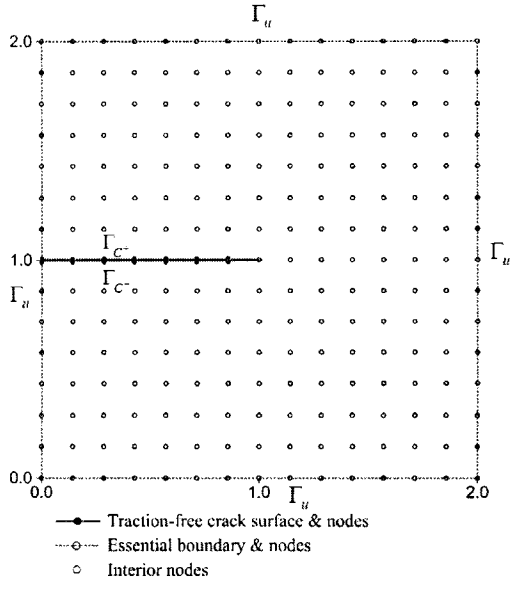

Figure 6. A regular node distribution with 232 nodes for near-tip crack problem.

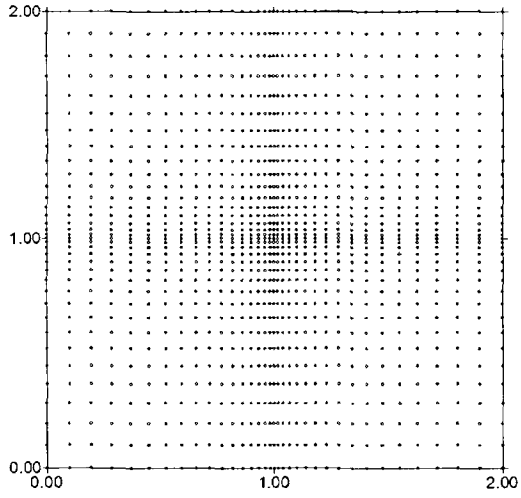

Figure 7. An adaptive node distribution with 1242 nodes for near-tip crack problem; node distributions with densification around the tip are used for the regular polynomial basis without enrichment where the aspect ratio $h_{\max}/h_{\min}$ is 10.

integral [18]. Table 2 presents the calculated stress intensity factors. The calculated stress intensity factors agree well with the prescribed value. In addition, the accuracy of modeling the Mode II near-tip field was studied. Similar to the Mode I case, the Mode II near-tip field with $K_{\mathrm{II}}^{\mathrm{pres}} = 1$ was applied along the patch boundaries. The errors in stress intensity factor computation were less than 0.1% for both Mode I and II cracks.

Table 2. Recalculated stress intensity factors for square patch with near-tip fields for Modes I and II. (Prescribed value of stress intensity factor is $K_{\mathrm{I}}^{\mathrm{pres}} = K_{\mathrm{II}}^{\mathrm{pres}} = 1\mathrm{psi}\sqrt{\mathrm{in.}}$)

Fracture Modes	Number of Nodes	Recalculated K_{I} and K_{II}	Relative Error (%)
Mode I	81	1.0002	0.02
	225	1.0003	0.03
	625	1.0001	0.01
Mode II	81	1.0007	0.07
	225	1.0002	0.02
	625	0.9999	0.01

To measure the error for our convergence studies, the relative error of the energy norm is used. A background mesh was used to evaluate the error integrals. The error is measured by

$$\|e\|_{\mathrm{energy}} = \frac{\left[\int_{\Omega} (\boldsymbol{\varepsilon}_{\mathrm{ex}} - \hat{\boldsymbol{\varepsilon}})^{\mathrm{T}} (\boldsymbol{\sigma}_{\mathrm{ex}} - \hat{\boldsymbol{\sigma}})\, d\Omega\right]^{1/2}}{\left[\int_{\Omega} \boldsymbol{\varepsilon}_{\mathrm{ex}}^{\mathrm{T}} \boldsymbol{\sigma}_{\mathrm{ex}}\, d\Omega\right]^{1/2}}, \tag{50}$$

where the superposed bar '^' stands for the numerical solution and the subscript 'ex' indicates the exact solution. Figure 8 shows the convergence rates for the relative energy error norms. For comparison, the convergence rates obtained by the regular quadratic, cubic, and quartic basis with irregular node distributions are also shown. The results for EFG methods with the exact derivatives and diffuse derivatives are also plotted (the basis of EFG method is intrinsically enriched). Note that the error for the enriched basis is much less than the others; however, the rate of convergence is not improved. Figure 9 shows the stress profile ahead of the crack tip at

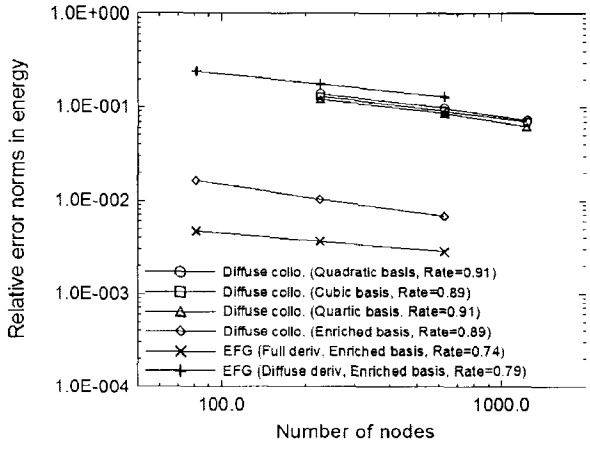

Figure 8. Convergence rates of relative energy norms for a square patch with near-tip field.

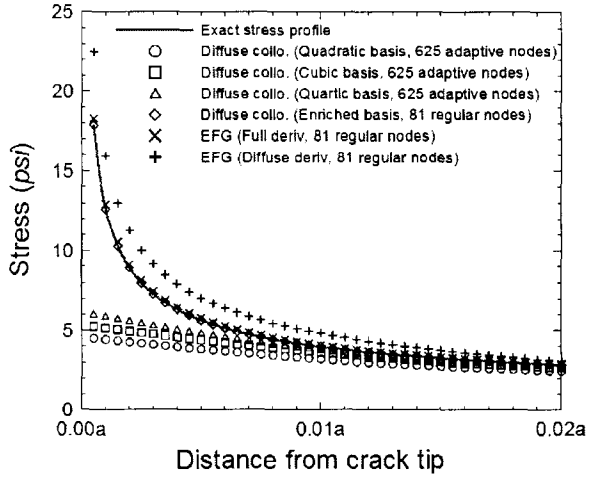

Figure 9. Comparison of profiles of near-tip stress to the closed form solution ranging from 0 to 0.02a.

$\theta = 0°$ for the 85 node model; for comparison, the results obtained by the unenriched polynomial basis with a 637 node model (with the aspect ratio $(h_{\max}/h_{\min})$ of 10) are also shown. Even as the sampling point $\mathbf{x}$ approaches the crack tip very closely, the enriched diffuse derivative approximation reproduces the exact profile pretty well. As a result, the singular behavior of stresses can be effectively captured.

In this method, the advantage over the Galerkin formulation results from the efficiency in computational cost. In Table 3, computation estimates of the meshfree collocation method and EFG methods with full and diffuse derivatives for constructing the discrete system are presented. For the operation counts, only multiplication is considered and the number of neighbor nodes is assumed to be three times of the dimension of $\mathbf{p}_m(\mathbf{x})$, namely, $3((n+m)!/n!m!)$. For example, operation counts for the meshfree collocation method, for EFG with diffuse derivatives and full derivatives, are given as about 1:10:20, respectively, when the following conditions are assumed: a two-dimensional $(n = 2)$ 100 node model; 3×3 Gauss quadrature of the weak form; linear basis for EFG $(m = 1)$ and quadratic basis for the meshfree collocation method $(m = 2)$. So, the computation of the discrete equations for the meshfree collocation method is less costly than that of EFG. However, the solution of the linear equations for large problems generally requires much time for linear elastostatics, so the overall difference tends to become smaller. For the moderately

Table 3. Operation counts of meshfree collocation method and EFG with full and diffuse derivatives in constructing the discrete systems where N_{nodes} is the total number of nodes; N_{GQP} is the number of Gauss quadrature points in a cell.

Methods	Operation Counts
Meshfree collocation method	$\left(4 \times \frac{(n+m)!}{n!m!}\right)^3 \times N_{\text{nodes}}$
EFG with diffuse derivative	$\left(4 \times \frac{(n+m)!}{n!m!}\right)^3 \times \{(\sqrt{N_{\text{nodes}}} - 1) \times N_{\text{GQP}}\}^2$
EFG with full derivative	$\left(5 \times \frac{(n+m)!}{n!m!}\right)^3 \times \{(\sqrt{N_{\text{nodes}}} - 1) \times N_{\text{GQP}}\}^2$

sized problems reported here, the computation of the discrete equations is a substantial part of the total run.

4.2. Growing Edge Crack under Tension

An edge-cracked specimen under uniform tension ($\sigma_y = 1$ psi) with a growing crack is considered (see Figure 10). The plate is in plane stress with Young's modulus $E = 3 \times 10^7$ psi and Poisson's ratio $\nu = 0.25$. A 502 node model with regularly distributed nodes is used. The crack increment of each step, Δa, is 0.5. As the crack grows from $a = 2.0$ in to $a = 5.0$ in, the evaluated stress intensity factors are plotted in Figure 11 with the analytic solution by Tada *et al.* [19]. The computed stress intensity factors show very good agreement with the analytic results.

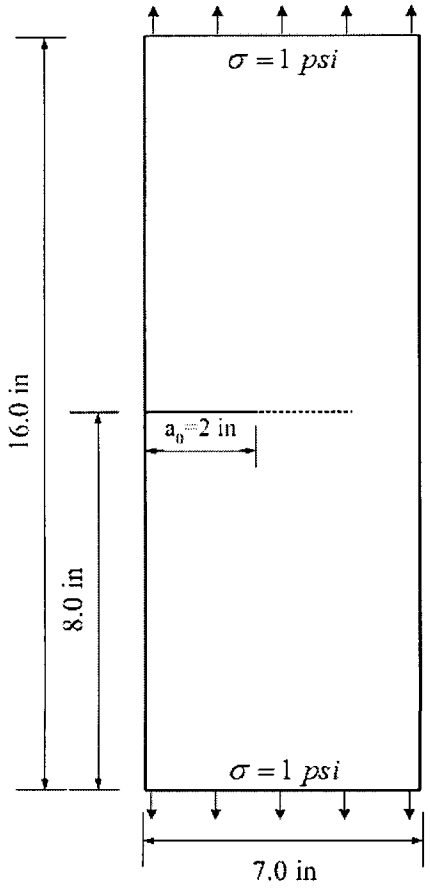

Figure 10. Problem illustration for edge-cracked specimen under tension.

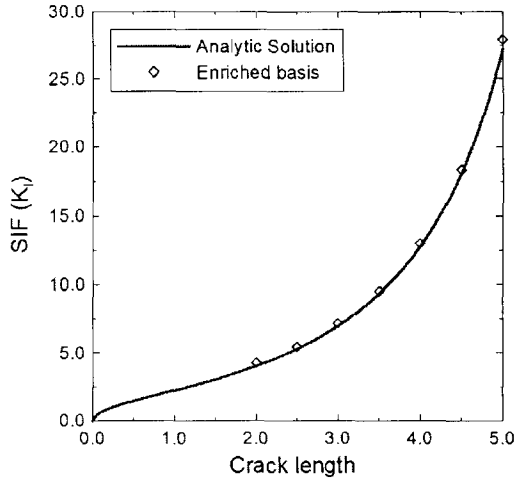

Figure 11. Mode I stress intensity factor as a function of the length of the crack.

4.3. Slant Edge Crack

A slant edge crack is considered to evaluate the methods for mixed mode cracks. Modes I and II stress intensity factors are evaluated for various lengths of an inclined crack. The plate is subjected to uniaxial tension of $\sigma = 1$ psi. (See Figure 12.) The dimensions of the plate are 8.0 in $\times$ 16.0 in, i.e., $H_1 = 8.0$ in, $H_2 = 8.0$ in, and $W = 8.0$ in. The length of the 45° inclined crack, a, varies from 2.55 in to 5.37 in. An 871 node model is used. For the evaluation of the interaction integral, a rectangular domain (2 in $\times$ 2 in) is used.

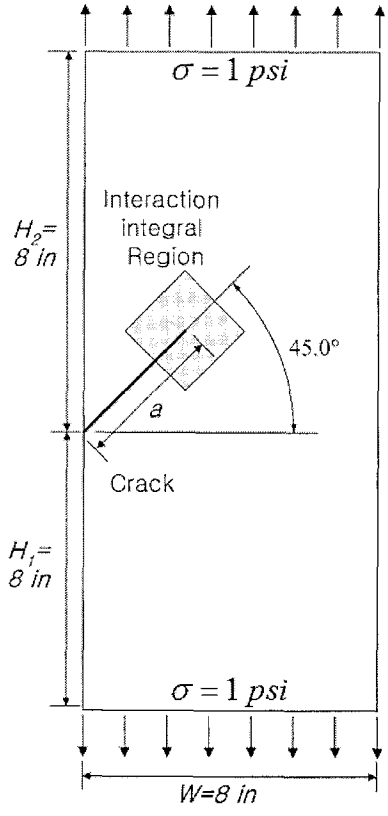

Figure 12. Edge slant cracked plate subjected to uniform uniaxial tensile stress.

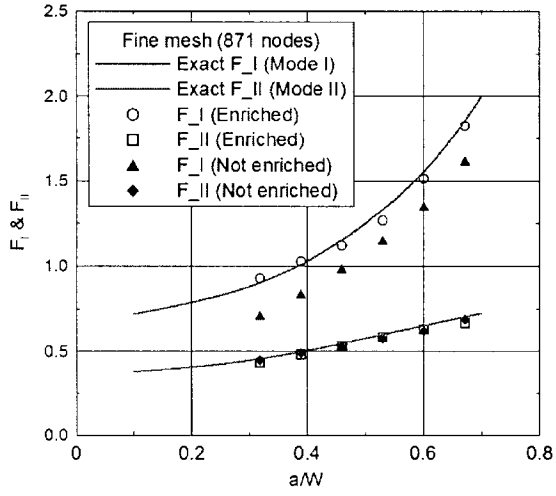

Figure 13. Normalized Modes I and II stress intensity factors for edge slant cracked plate subjected to uniform uniaxial tensile stress as a function of crack length a/W; the normalized stress intensity factors are computed by $F_{\mathrm{I}} = K_{\mathrm{I}}/\sigma\sqrt{\pi a}$ and $F_{\mathrm{II}} = K_{\mathrm{II}}/\sigma\sqrt{\pi a}$.

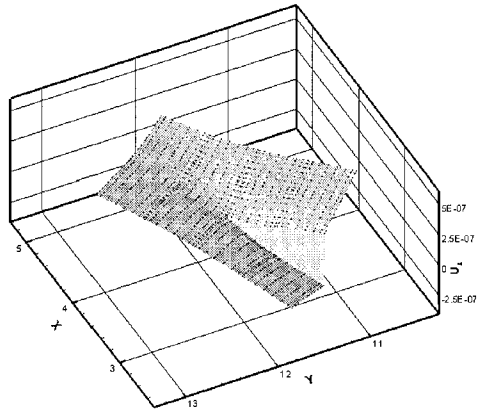

(a) $\hat{u}_1(\mathbf{x})$ (computed by quadratic polynomial basis without enrichment).

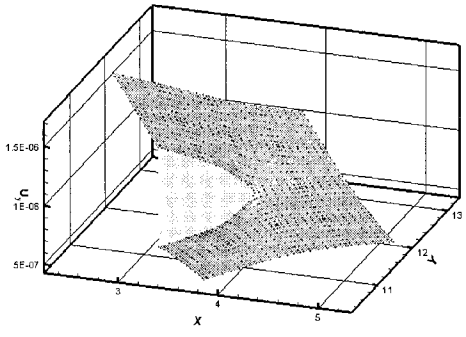

(b) $\hat{u}_2(\mathbf{x})$ (computed by quadratic polynomial basis without enrichment).

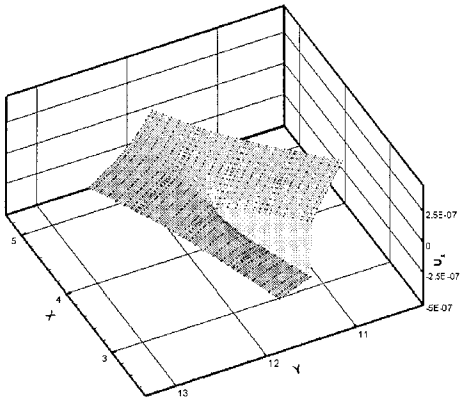

(c) $\hat{u}_1(\mathbf{x})$ (computed by the enriched diffuse derivative approximation).

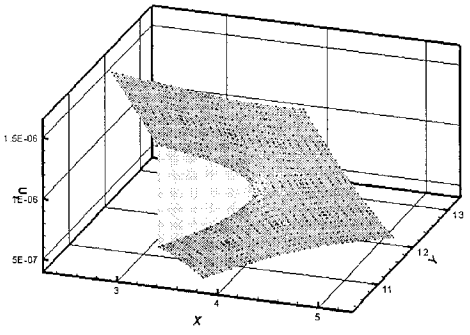

(d) $\hat{u}_2(\mathbf{x})$ (computed by the enriched diffuse derivative approximation).

Figure 14. Surface plots of displacements near the tip of slant crack.

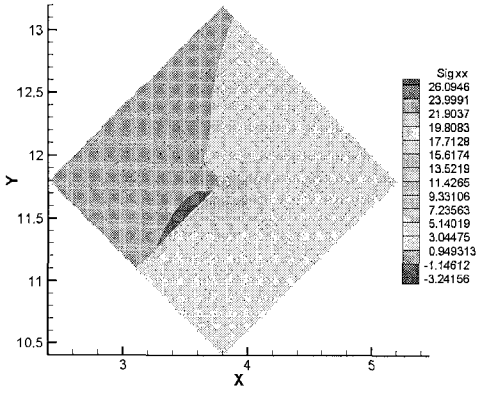

(a) $\hat{\sigma}_{11}(\mathbf{x})$ (computed by the quadratic polynomial basis without enrichment).

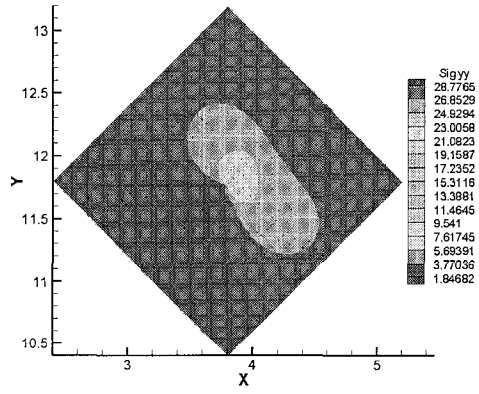

(b) $\hat{\sigma}_{22}(\mathbf{x})$ (computed by the quadratic polynomial basis without enrichment).

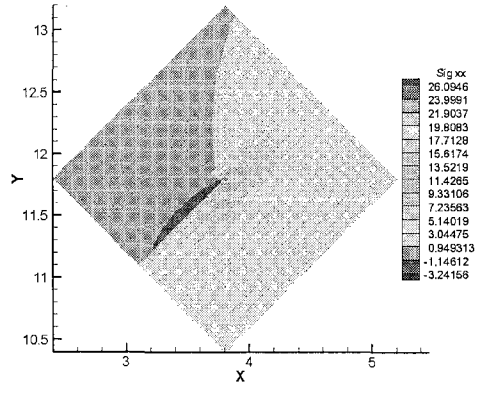

(c) $\hat{\sigma}_{11}(\mathbf{x})$ (computed by the enriched diffuse derivative approximation).

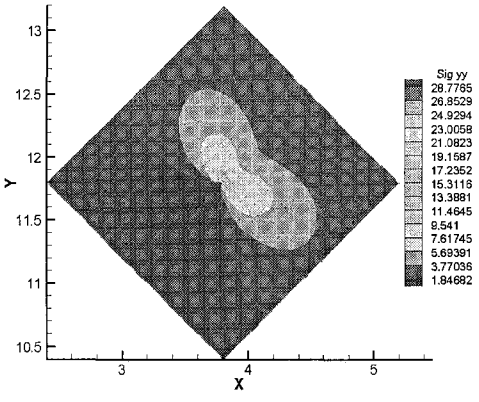

(d) $\hat{\sigma}_{22}(\mathbf{x})$ (computed by the enriched diffuse derivative approximation).

Figure 15. Contour plots for the stresses near the tip of slant crack.

In Figure 13, stress intensity factors for Mode 1 and Mode 2 are plotted as a function of crack length, a/W. The reference solutions given in [20] are also plotted for comparison. The enriched diffuse derivative approximation gives much better solutions than the unenriched approximation although the improvements for the Mode II stress intensity factors are not significant. Figures 14a and 14b show surface plots for the displacement near the crack tip, which are computed by the regular basis. The same domain as that used for computing the interaction integral is chosen for the plots. Figures 14c and 14d show surface plots of displacements near the tip computed by the enriched diffuse derivative approximation. Note that the profiles of the crack opening displacement, which should be parabolic, are successfully computed, while the profiles shown in Figures 14a and 14b obtained without enrichment are not parabolic. Similarly, contour plots for the stresses are presented in Figures 15a–15d. As seen in Figures 15c and 15d, the enriched approximation more effectively captures the singular behavior of the stresses.

5. CONCLUSIONS

An enriched meshfree method based on collocation with diffuse derivatives for solving elastic crack problems has been presented. The enriched approximation was constructed in the framework of diffuse derivatives and included the near-tip fields in the basis, often called in-

trinsic enrichment. The local behavior of the near-tip stresses was successfully modeled by the intrinsic enrichment. It is noteworthy that this approximation reproduces polynomials and the enrichment functions; this aspect was proven and verified in Section 2.2 with several numerical demonstrations.

To take advantage of merits of diffuse derivatives, the approximation was implemented in a collocation method. The method has several attractive aspects: consistent derivative approximations are obtained without differentiating the weight function or the moment matrix; a structured grid is not required for the construction of the approximation or the discretization of governing equations; no special treatment of the essential boundary condition is required. The governing partial differential equations were discretized directly at nodes in the domain and on the boundaries including crack surfaces.

Numerical experiments for elastic crack problems demonstrated the accuracy and robustness of the method. The near-tip field was effectively captured and accurate stress intensity factors were obtained. Compared to the unenriched approximations with node densification near the crack tip, the magnitude of the error was dramatically reduced. Growing crack problems were also solved. It is concluded that the intrinsic enrichment technique can be successfully combined with diffuse derivatives in collocation methods. While the accuracy does not quite match EFG for a given number of unknowns, the method is somewhat faster for elastic problems for a given accuracy. This approach can be extended to other types of intrinsic enrichment functions.

REFERENCES

1. M. Fleming, Y.A. Chu, B. Moran and T. Belytschko, Enrichment element-free Galerkin methods for crack tip fields, *International Journal for Numerical Methods in Engineering* **40**, 1483–1504, (1997).
2. T. Belytschko and M. Fleming, Smoothing, enrichment and contact in the element-free Galerkin method, *Computers and Structures* **71**, 173–195, (1999).
3. S.-H. Lee and Y.-C. Yoon, Meshfree point collocation method for elasticity and crack problem, *International Journal for Numerical Methods in Engineering* **61**, 22–48, (2004).
4. B. Nayroles, G. Touzot and P. Villon, Generalizing the finite element method: Diffuse approximation and diffuse elements, *Computational Mechanics* **10**, 307–318, (1992).
5. Y. Krongauz and T. Belytschko, Consistent pseudo-derivatives in meshless methods, *Computer Methods in Applied Mechanics and Engineering* **146**, 371–386, (1997).
6. Y. Krongauz and T. Belytschko, A Petrov-Galerkin diffuse element method (PG DEM) and its comparison to EFG, *Computational Mechanics* **19**, 327–333, (1997).
7. A. Huerta, T. Belytschko, S. Fernández-Méndez and T. Rabczuk, Meshfree methods, In *Encyclopedia of Computational Mechanics*, pp. 279–309, Wiley, (2004).
8. S. Li and W.K. Liu, Meshfree and particle methods and their applications, *Applied Mechanics Review* **55**, 1–34, (2002).
9. T. Belytschko, Y.Y. Lu and L. Gu, Element-free Galerkin methods, *International Journal for Numerical Methods in Engineering* **37**, 229–256, (1994).
10. T. Belytschko, L. Gu and Y.Y. Lu, Fracture and crack growth by element-free Galerkin methods, *Modeling Simulations in Materials Science and Engineering* **12**, 519–534, (1994).
11. T. Belytschko, Y.Y. Lu, L. Gu and M. Tabbara, Element-free Galerkin methods for static and dynamic fracture, *International Journal of Solids and Structures* **32**, 2547–2570, (1995).
12. T. Belytschko and M. Tabbara, Dynamic fracture using element-free Galerkin methods, *International Journal for Numerical Methods in Engineering* **39**, 923–938, (1996).
13. C.A. Duarte and J.T. Oden, Hp clouds and hp meshless method, *Numerical Methods for Partial Differential Equations* **12**, 673–705, (1996).
14. G. Ventura, J.X. Xu and T. Belytschko, A vector level set method and new discontinuity approximations for crack growth by EFG, *International Journal for Numerical Methods in Engineering* **54**, 923–944, (2002).
15. S.-H. Lee and Y.-C. Yoon, An improved crack analysis technique by element-free Galerkin method with auxiliary supports, *International Journal for Numerical Methods in Engineering* **56**, 1291–1314, (2003).
16. D.W. Kim and Y.-S. Kim, Point collocation methods using the fast moving least square reproducing kernel approximation, *International Journal for Numerical Methods in Engineering* **56**, 1445–1464, (2003).
17. G.E. Fasshauer, Solving partial differential equations by collocation with radial basis functions, In *Surface Fitting and Multiresolution Methods*, (Edited by A. LeMéhauté, C. Rabut and L. Shumaker), Vanderbilt University Press, Nashville, TN, (1997).
18. B. Moran and C.F. Shih, Crack tip and associated domain integrals from momentum and energy balance, *Engineering Fracture Mechanics* **27**, 615–641, (1987).

19. H. Tada, P.C. Paris and G.R. Irwin, *The Stress Analysis of Cracks Handbook*, Del Research, Hellertown, PA (1973).
20. Y. Murakami, *Stress Intensity Factors Handbook*, Pergamon, Oxford, (1986).